Lawrence Berkeley National Laboratory
Recent Work

Title
Electronic structure calculations permit identification of the driving forces behind frequency shifts in transition metal monocarbonyls.

Permalink
https://escholarship.org/uc/item/86h547pk

Journal
Physical chemistry chemical physics : PCCP, 22(2)

ISSN
1463-9076

Authors
Rossomme, Elliot
Lininger, Christianna N
Bell, Alexis T
et al.

Publication Date
2020

DOI
10.1039/c9cp04643g

Peer reviewed

Electronic Supplementary Information:

Electronic structure calculations permit identification of the driving forces behind frequency shifts in transition metal monocarbonyls

Elliot C. Rossomme,[†] Christianna N. Lininger,[†,‡,¶] Alexis T. Bell,[¶] Teresa Head-Gordon,[†,‡,¶] and Martin Head-Gordon[*,†,‡]

†*Kenneth S. Pitzer Center for Theoretical Chemistry, Department of Chemistry, University of California, Berkeley, California 94720, USA*

‡*Chemical Sciences Division, Lawrence Berkeley National Laboratory, Berkeley, California 94720, USA*

¶*Department of Chemical and Biomolecular Engineering and Department of Bioengineering, University of California, Berkeley, California 94720, USA*

E-mail: mhg@cchem.berkeley.edu

S1. MCO Geometries and Binding Energies

The main text of the article contains binding energies computed using def2-QZVPD[1,2] single-point energy computations on metal monocarbonyl (MCO) geometries optimized using the more tractable def2-TZVPD basis set.[2,3] Binding energies in the main manuscript also contain a vibrational zero-point energy correction (VZPE) using harmonic vibrational frequencies determined in the def2-TZVPD basis. Results from both coupled-cluster with single, double, and perturbative triple excitations [CCSD(T)][4] and ωB97X-V[5] density functional theory (DFT) computations were reported using this protocol. In an effort to facilitate more direct comparisons with subsequent computational studies, we include the def2-TZVPD energies both with and without VZPE in Table S1.

Table S1: Electronic, vibrational zero point, and binding energies for first-row transition metal monocarbonyls. Geometries and vibrational frequencies were determined using the def2-TZVPD basis set, and complex single-point energies using bases indicated in the table. Energies in kcal/mol.

| Species | CCSD(T) | | | | | ωB97X-V | | | | |
| | TZVPD | | | QZVPD | | TZVPD | | | QZVPD | |
	D_e	VZPE	D_0	D_e	D_0	D_e	VZPE	D_0	D_e	D_0
CO	–	6.17	–	–	–	–	6.40	–	–	–
TiCO$^-$	-60.82	7.83	-59.16	-82.17	-80.51	-32.05	7.44	-31.01	-30.24	-29.20
VCO	-18.09	7.66	-16.59	-18.68	-17.18	-19.26	7.73	-17.94	-18.90	-17.58
CrCO$^+$	-22.14	7.84	-20.47	-62.35	-60.68	-23.27	8.12	-21.55	-23.23	-21.51
VCO$^-$	-22.42	7.34	-21.25	-20.37	-19.20	-22.51	7.56	-21.35	-20.38	-19.22
CrCO	-2.83	6.89	-2.10	-3.03	-2.31	-3.19	7.09	-2.51	-3.18	-2.49
MnCO$^+$	-11.35	7.74	-9.78	-11.52	-9.95	-11.27	7.99	-9.68	-10.96	-9.38
CrCO$^-$	-0.21	6.09	-0.29	1.01	0.93	-2.77	6.42	-2.74	-1.72	-1.70
MnCO	22.12	7.92	23.87	18.83	18.75	10.78	8.21	12.59	11.04	12.85
FeCO$^+$	-36.02	8.15	-34.04	-38.05	-36.08	-35.94	8.43	-33.92	-35.61	-33.58
CoCO$^-$	-5.96	7.54	-4.8	-6.86	-5.49	-22.20	7.88	-20.72	-18.77	-17.29
NiCO	-38.09	8.71	-35.55	-42.06	-39.52	-33.53	8.76	-31.17	-32.94	-30.58
CuCO$^+$	-32.10	8.14	-30.12	-35.14	-33.16	-35.25	8.52	-33.14	-35.29	-33.17
NiCO$^-$	-19.35	6.87	-18.65	-27.90	-27.20	-25.02	8.21	-23.21	-21.42	-19.61
CuCO	-6.64	7.37	-5.44	-7.47	-6.27	-6.27	7.42	-5.25	-6.46	-5.44
ZnCO$^+$	-16.24	7.97	-14.42	-17.32	-15.50	-16.90	8.22	-15.08	-16.72	-14.90
^{1}CuCO$^-$	-1.75	6.41	-1.51	-1.43	-1.19	-1.98	6.69	-1.69	-1.30	-1.01
^{3}CuCO$^-$	9.43	6.79	10.05	11.14	11.76	6.24	7.03	6.87	8.08	8.71
^{1}ZnCO	-0.34	6.27	-0.24	-0.43	-0.34	-0.21	6.41	-0.20	-0.18	-0.18
^{3}ZnCO	54.05	7.97	55.85	54.53	56.34	52.93	8.24	54.77	52.65	54.49

S2. EDA Surfaces for MCO Anions

In the main text we argued that transition metal anions are unable to bind CO without the inclusion of charge transfer (CT) effects on the basis of energy decomposition analysis (EDA) surfaces for CoCO-. Here we extend this analysis through presentation of EDA surfaces for the remaining anions in this study and with a more detailed analysis of the electrostatic properties of CO.

S2.1. Additional Rigid-CO MCO$^-$ Surfaces

We computed present rigid-CO dissociation curves for Ti$^-$, V$^-$, Cr$^-$, Ni$^-$, Ni$^-$, and Cu$^-$ computed using the ωB97X-V functional[5] with the def2-TZVPD basis set.[2,3] Binding energies for FRZ, POL, and FULL, all defined in the main text, are presented for each species. In all cases we have used $r_{CO} = 1.126\,\text{Å}$, the equilibrium bond length for CO at this level of theory. For each species we plot the binding energy for linear (head-on) dissociation of the M$-$CO bond to facilitate more direct comparison between different species, despite the fact that CrCO$^-$ exhibits a bent ground-state structure (see discussion in Section 3.3.3 of the main text and references therein). Linear CrCO$^-$ is metastable with respect to its isolated fragments, but this does not affect our analysis in this section. These results are presented in Figure S1.

None of the anions in this study are found to exhibit bound structures on their FRZ and POL surfaces. This lack of M$-$CO bond formation is the result of both electrostatic repulsion between the metal anion and the negatively charged C-terminus of CO as well as the significant Pauli repulsion between the diffuse metal 4s- and CO 5σ-electrons. While orbital polarization diminishes the extent of this repulsion such that the POL surfaces are a rigorous lower bound of the FRZ surfaces (as they must be[6]), this effect is not significant enough to lead to binding. It is interesting to note that CO is able to achieve a closer approach to Cu$^-$ than to any of the other metal anions on both the FRZ and the POL
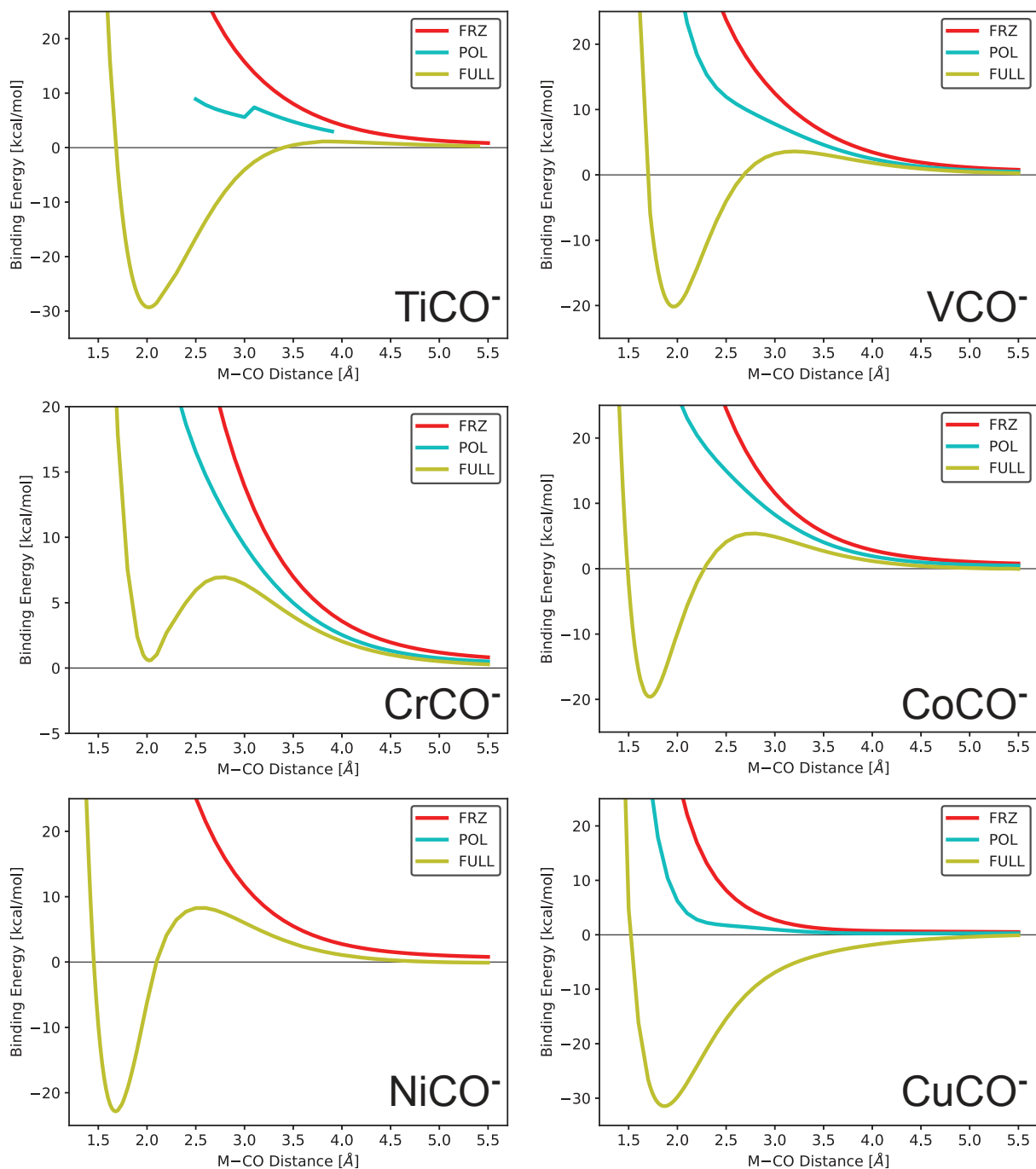
4

Figure S1: Adiabatic EDA surfaces for anionic transition metal monocarbonyls, obtained at the ωB97X-V//def2-TZVPD level of theory. None of the metal anions bind CO absent the inclusion of charge transfer, and all unconstrained surfaces but that for CuCO⁻ exhibit a repulsive wall at moderate M−C distances. The lack of complete POL surfaces for NiCO⁻ and TiCO⁻, as well as the discontinuity in the latter, are due to difficulties in converging SCF iterations to the appropriate solution.

5

surfaces. While this is in part due to the more compact metal valence orbitals promoted by a higher nuclear charge, this is likely also a feature of the fact that Cu^- binds CO through an $[Ar]3d^{10}4s^14p^1$ configuration (see main text), and the $4p$-orbital has less spatial overlap with the 5σ-orbital.

Once the effects of CT have been included, bound structures for all of the anions are achieved. Even still, the features that prohibit binding on the FRZ and POL surfaces are manifest in all of the PESs presented in Figure S1. As CO approaches a metal anion, the interaction is initially destabilizing, and the fragments repel each other because of permanent electrostatics and Pauli repulsion. Once a sufficiently close approach between the fragments is achieved, CT between fragments ensues and a stable complex can form. Based on results of previous studies,[7] it seems likely that this stabilization is due to both the diminishing of Pauli repulsion and energetically favorable orbital mixing. Again, $CuCO^-$ exhibits a fundamentally different binding phenomenology than the other anions, and no initial barrier to Cu^--CO bond formation is observed. This provides additional evidence that the $4p \leftarrow 4s$ promotion diminishes inter-fragment Pauli repulsion significantly.

S2.2. The Effect of C−O Stretching on MCO⁻ Binding

A naïve view of electrostatics leads one to expect repulsion between metal anions and equilibrium ($r = 1.126\,\text{Å}$) length CO, the latter of which possesses a slight negative charge on the carbon atom: like charges repel each other. However, as noted in the main text, low-energy extensions of the CO bond can reverse the sign of the dipole, placing a slight positive charge on the carbon end of CO (Figure 3 in the main text). In light of this, we also investigated whether a bound MCO^- structure could be obtained on dissociation curves constructed with an elongated CO bond (Figure S2). While stretching CO leads to marginal decreases in fragment repulsion, a bound structure between the fragments could not be realized, even when the perturbations to the CO bond were significant ($\Delta r \approx 0.08\,\text{Å}$; $\Delta E \approx 10\,\text{kcal/mol}$).

We rationalize this lack of binding on the basis of both Pauli repulsion between the frag-

ments and the distortion energy that accompanies CO stretching. The $3d$- and (if occupied) $4s$-orbitals of metal anions are relatively diffuse and therefore hinder a close approach between the two fragments, overpowering the small but stabilizing charge-dipole interaction between the metal anion and stretched CO. Continued stretching of CO is not expected to overcome this Pauli repulsion, as linear increases in the CO dipole moment correspond to quadratic increases in the CO fragment energy, rendering the energetic costs of increasing the dipole insurmountable. Hence, metal anions are unable to bind CO through the physical interactions included in the FRZ term of our EDA, in spite of the dipolar properties of CO described in the main text.
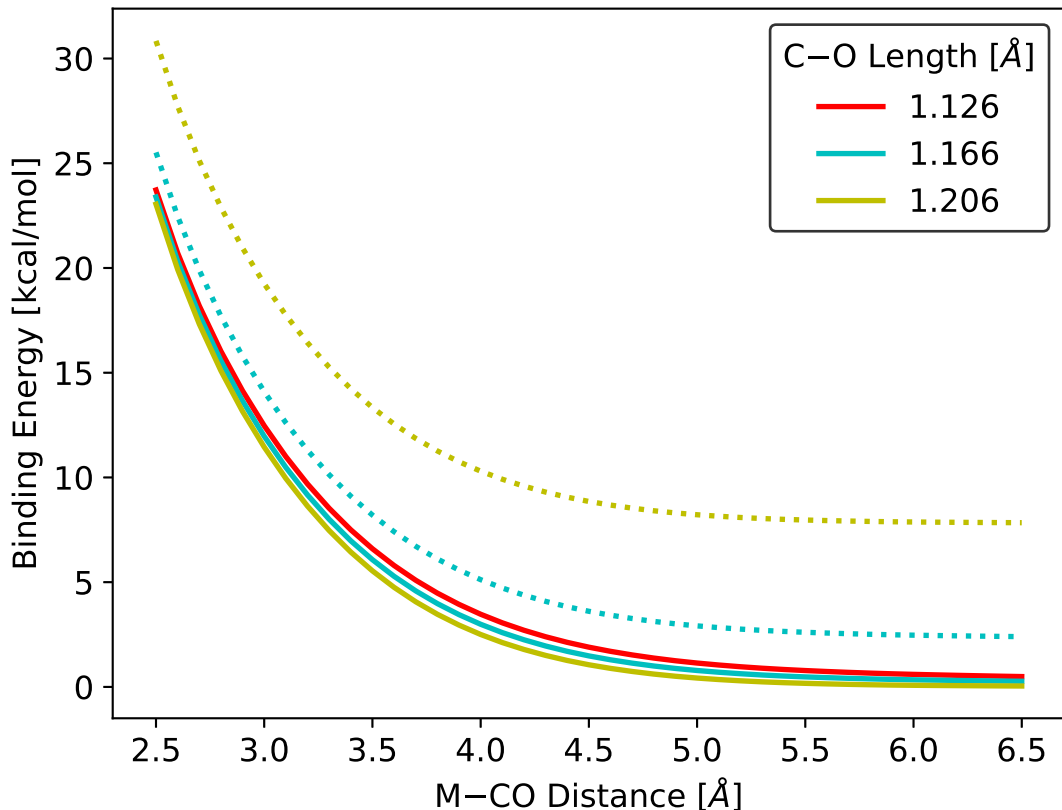

Figure S2: Potential energy surfaces for VCO^- dissociation at different values of r_{C-O}. All dissociations are rigid in the $C-O$ bond length. The energetic zero for solid lines is defined as infinitely separated V^- and CO fragments, where the isolated fragment value for r_{C-O} is given by the colors in the legend. Dashed lines are rescaled such that the energetic zero corresponds to infinitely separated V^- and CO with $r_{C-O} = 1.126$ Å.

S3. Subtleties in MCO Binding

The main text provides a broad strokes model of MCO binding that accounts for general experimental trends well. This general model is adequate for anionic MCOs, but both neutral and cationic systems exhibit more subtle trends. These additional features of experimental data on neutral and cationic metals can likely be understood on the basis of metal atom electron configurations. We include conjectures to this effect here.

Our model of cation binding indicates that FRZ and POL interactions drive moderate to large values of ΔE_{bind} and significant blue shifts in ω_{CO}. CT provides additional stabilization to these complexes and also attenuates the blue-shifting tendencies of interaction with the cation. Additional subtleties in the trends in ΔE_{bind}, $r_{\mathrm{M-C}}$, and ω_{CO} for MCO cations can be understood in terms of the orbital occupation of the isolated metal fragment. As suggested by the CT results, discussed in the main text, two classes of MCO cations are apparent in our data set. These are $MnCO^+$ and $ZnCO^+$ on the one hand and $CrCO^+$, $FeCO^+$, and $CuCO^+$ on the other. In the former case the coupled occupied-valence pair (COVP) analysis indicates that back-donation is all but absent, whereas it contributes to the stability and ω_{CO} red-shifting in the latter. The extent of back-donation is correlated with $r_{\mathrm{M-C}}$ (see Table 2): longer M$-$C bonds diminish spatial overlap between the orbitals involved in back-donation.

It seems plausible that electron configuration of the isolated metal cation, particularly the occupancy of the diffuse $4s$-orbital, governs the closeness of CO approach in the complex. In ground state $^6Cr^+$, $^4Fe^+$, and $^1Cu^+$, the $4s$-orbital is unoccupied, allowing for relatively short M$-$C bonds. Similarly short M$-$C bonds are prevented by the occupation of the $4s$-orbital in the ground state configurations of $^7Mn^+$ and $^2Zn^+$. Within each of these two classes of metal cations, the ordering of the M$-$C bond lengths follows the general trend of decreasing atomic radius across the periodic table due to increasing nuclear charge. In essence, metal electron configurations determine the closeness of M$-$CO approach and thereby the extent of spatial orbital overlap, which controls the amount of back-donation in the complex. This

analysis cannot account for the cation frequency shifts in their entirety. For instance the red shift in $FeCO^+$ due to charge transfer is significantly larger than that for $CuCO^+$, despite similar M−C bond lengths. Still, metal cation electron configurations and their influence on r_{M-C} can serve as a touchstone for understanding the nature of charge transfer in their carbonyl complexes.

Neutral MCOs are generally more complicated than their ionic counterparts, such that producing a coherent model of their binding is more difficult. Still, as in the cationic species, the magnitude of both ΔE_{bind} and $\Delta\omega_{CO}$ generally correlates with the occupancy of the $4s$-orbital. VCO and NiCO, which do not have $4s$-electrons, exhibit the most significant CT contributions to their binding. Charge transfer in these two complexes leads to more than $200\,cm^{-1}$ red shifts in ω_{CO} (Table 4) and large decreases in ΔE_{bind} (Table 3). The contribution to ΔE_{bind} is particularly large for NiCO, where an exceptionally short ($1.680\,Å$) M−C bond creates significant overlap between the fragment orbitals, resulting in nearly $40\,kcal/mol$ of additional complex stabilization. Single occupation of the $4s$-orbitals in CrCO and CuCO directly limits forward donation and, more importantly, indirectly limits back donation by diminishing the overlap between the relevant orbitals. Hence, less significant stabilization energies (3–$6\,kcal/mol$) and frequency shifts (120–$125\,cm^{-1}$) are seen in most neutral as compared to ionic MCOs.

S4. Charge Delocalization in NiCO Surfaces

Mulliken population analyses reveal charge delocalization errors[8] for structures corresponding to the NiCO EDA surfaces, presented in Figure 7(a) in the main text. Spurious charge delocalization results in two different asymptotes for Ni−CO bond stretching: one for the FRZ and POL surfaces, and another for the unconstrained surface.

The POL surface exhibits a discontinuity between 2.6 and 2.7 Å, across which the sign of the charge delocalization changes. Examination of molecular orbitals on this surface explains
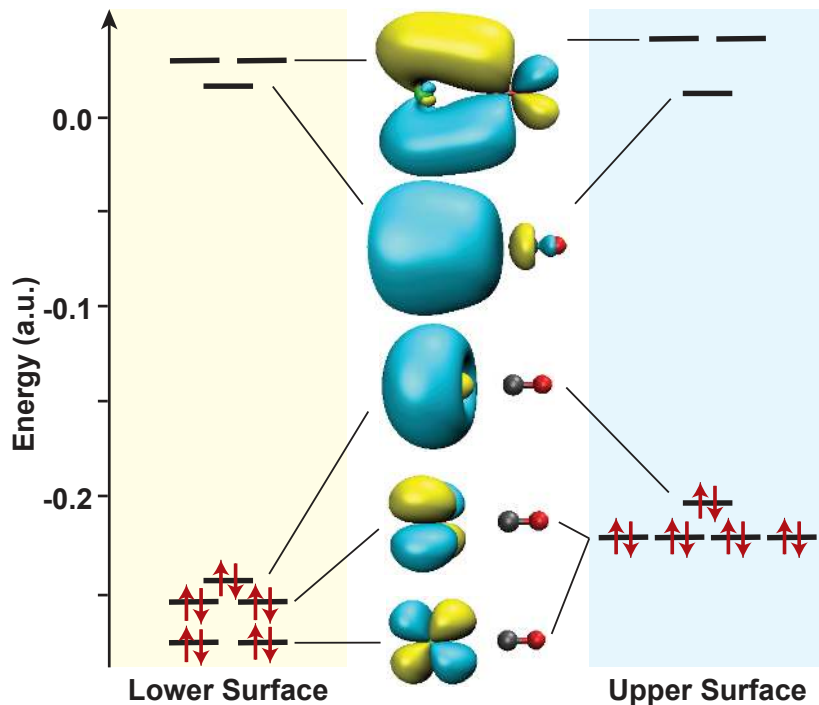
Figure S3: Molecular orbital diagram for POL surface of ^{1}NiCO (see Figure 7(a) in the main text). The orbitals on the lower and upper surfaces were obtained with $r_{\mathrm{M-C}} =$ 2.7 and 2.8 Å, respectively.

the source of this discontinuity (Figure S3). In the limit of a large separation between the fragments, the $3d$-orbitals in ^{3}Ni will be 10-fold degenerate. The degeneracy in these orbitals is lifted upon approach of the CO adsorbate. The plots in Figure S3 indicate that this degeneracy is first lifted as the $3d_{z^2}$ orbital polarizes, likely due to the CO 5σ-electrons, and then is further lifted as the $3d_{xz}$ and $3d_{yz}$ orbitals polarize to accommodate the π-electrons. The discontinuity in the POL surface in Figure 7(a) is apparently due to the lifting of this degeneracy as CO approaches ^{1}Ni from $r_{\mathrm{M-C}} = 2.8$ Å. All FRZ computations yielded binding energies on the "upper" surface, which corresponds to a ^{1}Ni atom with 2- and 8-fold degeneracy among the $3d$-orbitals. The persistence of this degeneracy across the $r_{\mathrm{M-C}}$ values of interest is due to the mechanics of the FRZ computation, which completes the SCF iterations for each fragment independently of the other (*i.e.* intramolecular relaxation due to the presence of other fragments is prevented).

10

Notably, none of our computations recover the 10-fold degeneracy of the Ni d-orbitals at large values of $r_{\text{M-C}}$, and both asymptotes are therefore spurious. This feature of our computational approach, due to charge delocalization errors, does not necessarily invalidate the results obtained in the short M−C regime. As the energies of all optimized structures were found to be stable with respect to rotations between the occupied and virtual orbital subspaces, we take these results to be legitimate. Using these results, the binding energies presented in Table 5 were obtained with respect to the isolated fragments, which lie slightly above the energy of the upper asymptote in Figure 7(a).

References

(1) Weigend, F.; Furche, F.; Ahlrichs, R. Gaussian basis sets of quadruple zeta valence quality for atoms H-Kr. *J. Chem. Phys.* **2003**, *119*, 12753–12762.

(2) Rappoport, D.; Furche, F. Property-optimized Gaussian basis sets for molecular response calculations. *J. Chem. Phys.* **2010**, *133*, 134105.

(3) Weigend, F.; Ahlrichs, R. Balanced basis sets of split valence, triple zeta valence and quadruple zeta valence quality for H to Rn: Design and assessment of accuracy. *Phys. Chem. Chem. Phys.* **2005**, *7*, 3297–3305.

(4) Raghavachari, K.; Trucks, G. W.; Pople, J. A.; Head-Gordon, M. A fifth-order perturbation comparison of electron correlation theories. *Chem. Phys. Lett.* **1989**, *157*, 479–483.

(5) Mardirossian, N.; Head-Gordon, M. ωB97X-V: A 10-parameter, range-separated hybrid, generalized gradient approximation density functional with nonlocal correlation, dsigned by a survival-of-the-fittest strategy. *Phys. Chem. Chem. Phys.* **2014**, *16*, 9904–9924.

(6) Mao, Y.; Horn, P. R.; Head-Gordon, M. Energy decomposition analysis in an adiabatic picture. *Phys. Chem. Chem. Phys.* **2017**, *19*, 5944–5958.

(7) Ziegler, T.; Tschinke, V.; Ursenbach, C. Thermal stability and kinetic lability of the metal–carbonyl bond. A theoretical study on $M(CO)_6$ (M = Cr, Mo, W), $M(CO)_5$ (M = Fe, Ru, Os), and $M(CO_4)$ (M = Ni, Pd, Pt). *J. Am. Chem. Soc.* **1987**, *109*, 4825–2837.

(8) Cohen, A. J.; Mori-Sánchez, P.; Yang, W. Challenges for density functional theory. *Chem. Rev.* **2012**, *112*, 289–320.